AIAA SciTech Forum
6-10 January 2025, Orlando, FL
AIAA SCITECH 2025 Forum

10.2514/6.2025-1226

Design and Analysis of Ceramic-Halide Heat Pipes for Intermediate Temperature Systems

Andrew van Paridon*, Mathieu Boyer†, Giancarlo D'Orazio‡, and Sadaf Sobhani§

Liquid halides have been identified as promising working fluids for heat pipes operating in the intermediate temperature regime of 500–750 K. However, their compatibility with conventional heat pipe envelope materials remains limited. Ceramic heat pipes have been proposed as a solution, enabling compatibility with halide fluids while leveraging additive manufacturing for advanced topological designs. The design of aluminum nitride (AlN) heat pipes in the context of spacecraft radiators is analyzed, using aluminum bromide ($AlBr_3$) as the working fluid. A 1D thermal model of the combined radiator and heat pipe assembly is presented, optimized globally to achieve an areal density below 3 kg/m^2 while maintaining 70% radiator efficiency. This optimization yields a power density of 5 kW/m^2 and a heat rejection specific mass of 0.47 kg/kW. A range of potential designs is proposed, highlighting the refinement opportunities provided by additive manufacturing.

I. Nomenclature

$A_{c/f/\mathrm{tot}}$	=	Area (m^2) *Condenser / Fin / Total*
$A_{w/v/x}$	=	X-section Area (m^2) *Wetted / Vapor / Fin*
K	=	Permeability (m^2)
M	=	Merit Number (-)
P_v	=	Vapor Pressure (Pa)
Q	=	Heat Flow (W)
T	=	Temperature (K)
W	=	Fin Width (m)
c_p	=	Specific Heat Capacity (J/kg/K)
d_m	=	Mesh Screen Diameter (m)
h_{fg}	=	Enthalpy of Vaporization (J/kg)
k	=	Thermal Conductivity (W/m/K)
l	=	Length (m)
l_{eff}	=	Effective Length (m)
m	=	Mass (kg)
r	=	Radius (m)
r_{eff}	=	Effective Pore Radius (m)
s	=	Wick Groove Spacing (m)
t	=	Time (s)
$t_{r/t}$	=	Fin Root/Tip Thickness (m)
w	=	Groove Width (m)
w_m	=	Mesh Screen Width (m)
x	=	Distance Along Fin (m)
β	=	Heat Rejection Specific Mass (kg/kW)
ϵ	=	Emissivity (-)
η	=	Radiator Efficiency (-)
μ	=	Viscosity (Pa·s)
ρ	=	Density (kg/m^3)
ρ_A	=	Areal Density (kg/m^2)
σ	=	Surface Tension (N/m)
σ_{SB}	=	Stefan-Boltzmann Constant (W/m^2/K^4)
ϕ	=	Power Density (kW/m^2)
ψ	=	Porosity (-)

II. Introduction

Nuclear propulsion systems are a promising technology for interplanetary travel, particularly for crewed missions to Mars, as highlighted in NASA's Mars Transport Assessment Study [1]. Two main types of nuclear propulsion are under investigation: nuclear thermal propulsion (NTP) and nuclear electric propulsion (NEP). While NTP systems are relatively mature, NEPs require significant advancements to elevate their technology readiness levels. The nuclear reactors operate at temperatures between 1000 and 1800 K and, after power conversion, must dump the waste heat at approximately 500–700 K. Typically, a pumped fluid loop would deliver this heat to an array of radiators as shown in Fig. 1. Novel heat pipe and radiator concepts are crucial to furthering the efforts towards manned space exploration.

*Senior Lecturer & Research Associate, Sibley School of Mechanical and Aerospace Engineering, 141 Upson Hall, 124 Hoy Rd., Ithaca, NY 14853, and AIAA Member
†Graduate Student, Sibley School of Mechanical and Aerospace Engineering
‡Graduate Student, Sibley School of Mechanical and Aerospace Engineering, 184 Grumman Hall, 134 Rhodes Dr., Ithaca, NY 14853
§Assistant Professor, Sibley School of Mechanical and Aerospace Engineering, 141 Upson Hall, 124 Hoy Rd., Ithaca, NY 14853, AIAA Member

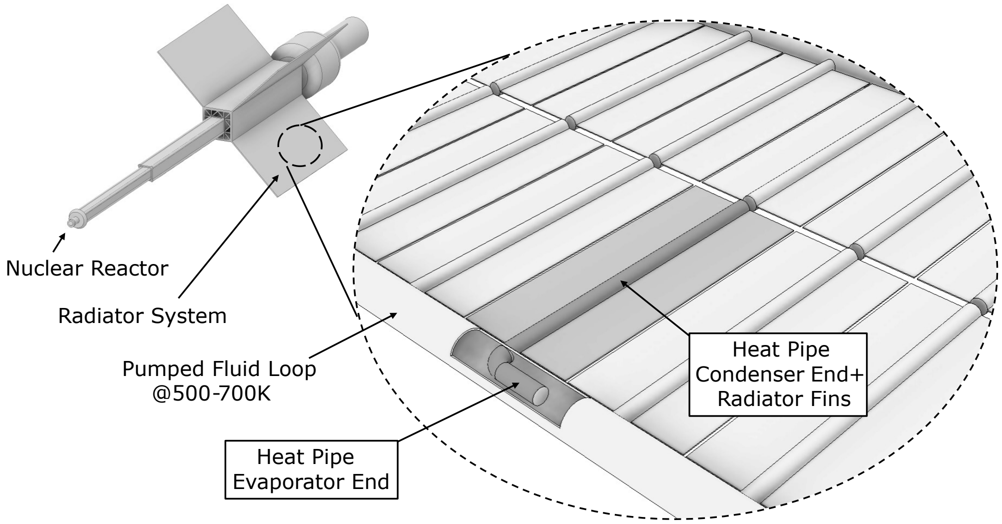

Fig. 1 Embedded heat pipe radiator network as part of NEP spacecraft thermal subsystem.

Despite their importance, a technology gap exists for heat pipes capable of reliable operation within the 'intermediate' temperature range 500-750 K. For many typical working fluids, this range is either near the critical temperature or below the freezing point (see Fig. 2) [2]. Many other working fluids, both organic and non-organic, have been examined with various levels of success. A comprehensive review has been prepared by Werner et al [3]. In particular, halides are of great interest due to their stability at these intermediate temperatures and high merit number [4]. Merit number is a ratio of the positive and negative fluid properties concerning thermal transport;

$$M = \frac{\rho_l \sigma h_{\text{fg}}}{\mu_l} \tag{1}$$

Anderson et al. [5] performed and reported on life tests concerning a number of halides, and noted in particular the capability of aluminum bromide ($AlBr_3$) to feasibly operate up to 673K. Werner et al. [3] found antimony tribromide ($SnBr_3$) to be one of the strongest candidates for investigation. They also point out that the literature concerning completed saturation tables of many halides have not been published.

While these halide working fluids hold promise for intermediate temperature systems, they are typically corrosive and require specific metal envelope material pairings [5]. Ceramics are therefore of great interest in order to broaden material compatibility with a spectrum of otherwise corrosive materials while also maintaining thermal stability at temperatures well above many metals. High temperature tolerance and chemical stability has appeal in the use of various heat exchanger designs[6] and more recently, additive manufacturing processes have enabled considerably more complex morphologies[7], just as hybrid wick structures have started to show promise in space based heat pipe design [8].

In terms of heat pipe envelope material, there are considerably fewer proven ceramic designs. A silicon-silicon carbide cermet was tested with zinc working fluid by Hack et al. [9] however this design is intended for high temperature operation. Sixel et al. developed a spherical alumina sintered wick which was trialed in an open evaporator configuration for testing at low temperature[10, 11]. Recently, Agrawal et al. developed an additively manufactured alumina oscillating heat pipe which was also tested in a low temperature system[12]. There remains a considerable gap in research as few, if any, ceramic heat pipe designs have been tested at intermediate temperatures.

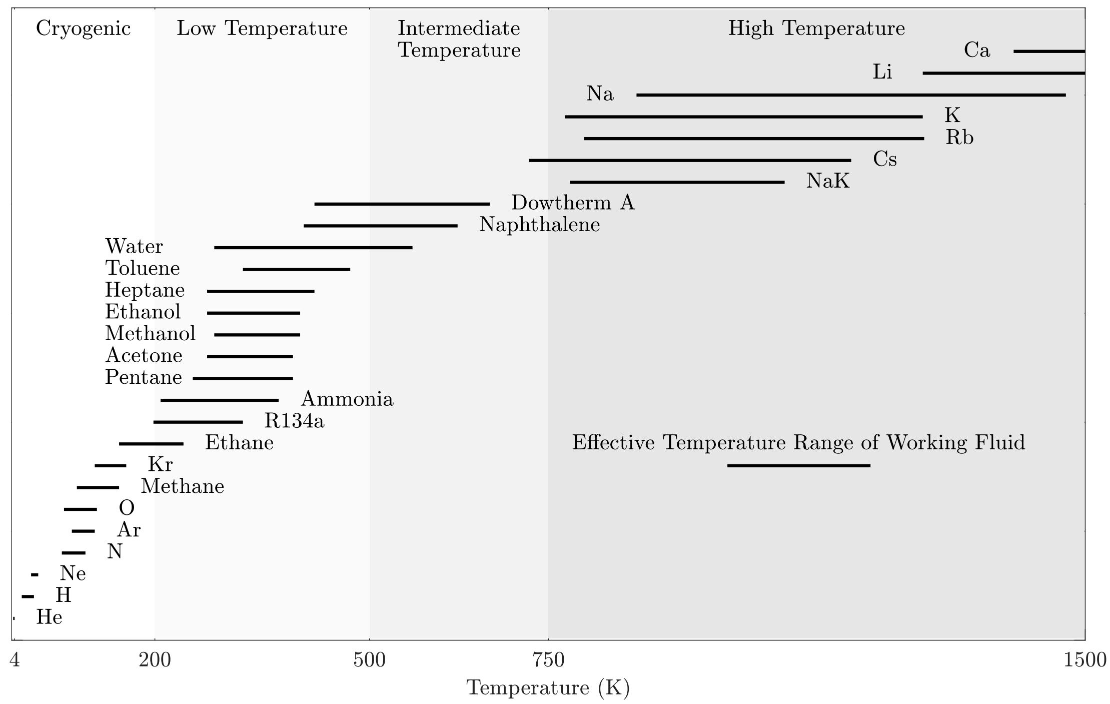

Fig. 2 Useful temperature range for common heat pipe working fluids. Data from Faghri 2018 [2].

Parallel efforts to numerically simulate heat pipe performance are necessary to guide and support the experimental effort. A comprehensive review of heat pipe modeling and optimization has been prepared by Tian et al [13]. Depending on the fidelity required, these range from lumped parameter to conjugate three-dimensional transient heat and mass transfer. The core of these models is establishing the heat pipe performance limits (such as capillary, boiling, entrainment, sonic, viscous) based on heat pipe geometry and working fluid thermofluid properties [14]. With these limitations, the functional operating regime for a given heat pipe geometry and corresponding working fluid can be determined. A full discussion of these limitations is presented in Section IV.D.

Simulation of integrated heat pipe - radiator designs has also seen continued effort. Furukawa developed a model of a network of linked radiators in order to optimize and manage the temperature of the pumped fluid loop system [15]. Hull et al. developed a genetic algorithm towards the same goal, to reduce the overall mass of the system in order to establish a strong foundation for interplanetary spacecraft [16]. Juhasz focused efforts on a combined heat pipe and radiator system that would be as light as 1.45kg/m^2 using carbon composites for the fins [17].

As presented by D'Orazio et al. [18], we have been investigating possible working fluids enabled by alumina and aluminum nitride (AlN) ceramic heat pipes, and down selected away from iodine for its reactivity. In the present work is a description of a 1D thermal model of a combined heat pipe radiator. This model is useful for predicting the performance of possible full scale designs, as well as the performance of the small scale lab prototypes. The base model was initially described by Van Paridon et al. [19], and here the model is extended to include variable radiator thickness and additional radiator materials. Finally, in complimentary work, we investigate the manufacturing process and initial performance for alumina heat pipes, including rate-of-rise testing to validate the wick permeability figures [20].

III. Material Properties

Titanium-Water heat pipes represent the state-of-the-art for heat pipes operating around 500 K. Above this, however, the effectiveness of water declines rapidly as the conditions approach the critical temperature (647 K). In this work we will explore the performance of aluminum bromide ($AlBr_3$) coupled with an Aluminum nitride (AlN) shell. A selection of thermal properties for envelope materials and working fluids is provided in Tables 1 and 2, respectively.

Aluminum nitride (AlN) has excellent thermal properties with relatively high thermal conductivity (>120 W/m·K), low bulk density, and high thermal shock resistance. It also has proven to be compatible with a number of working fluids from the halide group [5].

Table 1 Thermodynamic properties of envelope materials.

Material	Formula	Process	Heritage	T_m K	ρ kg/m^3	c_p J/kg·K	k_l W/m·K	σ_y MPa
Titanium (C.P.)	Ti	Milled	Legacy	1941	4510	528	21	880
Aluminum Nitride	AlN	Printed	Novel	2473*	3255	734	80-120*	300-500*

*Estimated

Table 2 Thermodynamic properties of working fluids.

Fluid	T_m	T_b K	T_c	h_{fg} kJ/kg	P_v MPa	ρ_l kg/m^3	μ_l	μ_v cP	k_l W/m·K	σ N/m
$AlBr_3$	371	528	763	172	0.177	2111	0.609	0.0205	0.0879	0.0107
H_2O	273	373	647	1376	6.13	755	0.097	0.019	0.580	0.0197
Dowtherm A	—	530	770	286	0.169	831	0.27	0.01	0.0976	0.0162

$\mapsto$ Evaluated at @T_{ref} = 550K as required.

IV. Heat Pipe and Radiator Modeling

A. Overview

The following model evaluates a heat pipe that accumulates thermal power at the evaporator and conducts it via the condenser to a radiative surface that is open to the space environment. The objective of the model is to evaluate the performance limits of a particular heat pipe design, find the optimal working temperature, and ensure consistency with the radiated heat. The full radiator surface comprises two fins and the outer surface of the condenser. Figure 3 shows an highlights the scope of the model in relation to the representative geometry.

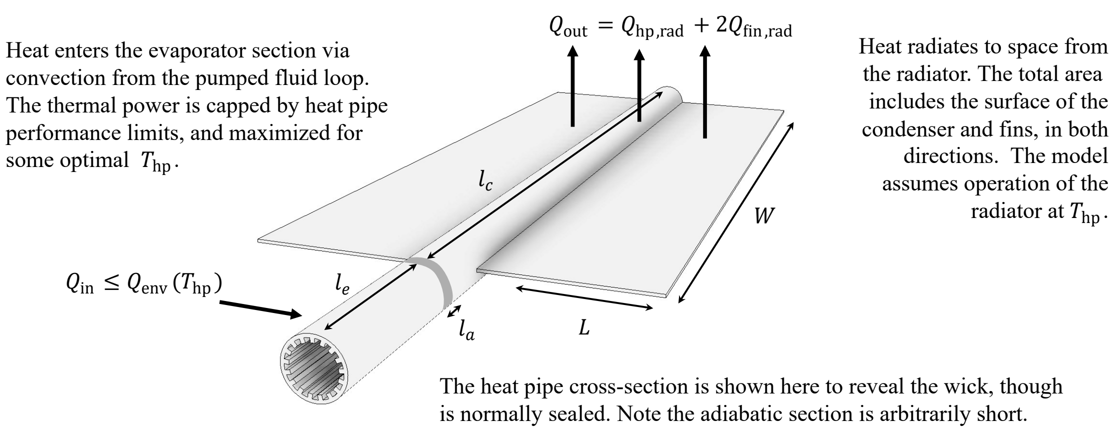

Fig. 3 Overview of the combined heat pipe and fin construction.

Heat pipes transport heat through the evaporation, transmission, and condensation of a working fluid. The fluid circulates from end-to-end; initially boiling in the evaporator, the vapor is driven by pressure towards the condenser section, where it condenses again into the annular wick structure, returning to the evaporator through capillary action. The pressure in the evaporator is created by surface tension at the fluid-vapor boundary and increases as heat is applied. The working fluid is maintained in a saturated state and sealed from the environment, allowing for a broad range of operating conditions.

Operating normally, heat pipes represent a very low thermal resistance within the grander thermal subsystem, and can be considered nearly isothermal. Heat transport is limited by a number of mechanisms that restrict the flow along different sections of the fluid pathways. Therefore, modeling these performance limits directly is sufficient to reasonably approximate the envelope of working conditions in lieu of higher order conjugate-CFD analysis. It can often be of similar effort to prototyping and testing. A full discussion of HP performance limits is available from Faghri [2].

Conversely, the heat conducted along the length of a radiator fin is restricted by the cross-sectional area and the conductivity of the material, so there is a significant temperature difference between the root and tip. This model evaluates the heat radiated by two fins that are in direct contact with the condenser length of the heat pipe, as well as the heat radiated from the condenser surface itself.

At each design iteration, the overall performance of the system is evaluated for a number of parameters that are important for practical application. These parameters will be discussed here, and an algorithm for optimizing them performance will be described in the following section.

B. Input Variables

The heat pipe and radiator geometry is shown in Fig. 4 and the relevant input parameters and implicit variables listed in Table 3. The model's wick design has been typically evaluated with grooved channels for prototype designs in bench-top testing, and with a combined grooved channel and mesh screen liner for evaluating full-scale design concepts. The fin has been evaluated using the same material as the heat pipe (assuming additively manufactured together) or from a different material. The thickness of the fin can be constant, or narrow towards the tip either linearly or parabolically.

Table 3 Input variables for heat pipe and radiator fin geometry.

Input Variables	Heat Pipe Geometry						Radiator Geometry	
	l_e	Evaporator Length	r_o	Outer Radius	w	Groove Width	L	Length
	l_a	Adiabatic Length	r_e	Envelope Radius	s	Groove Spacing	t_r	Root Thickness
	l_c	Condenser Length	r_i	Inner Radius	w_m	Mesh Width	t_t	Tip Thickness
					d_m	Mesh Diameter		
Implicit Variables								
	l_t	Total Length $= l_e + l_a + l_c$	A_w	Wick Wetted Area $= \pi(r_e^2 - r_i^2)$	d	Groove Depth $= r_e - r_i$	W	Radiator Width $= l_c$
	l_{eff}	Effective Length $= (l_e + l_c)/2 + l_a$	A_v	Vapor Core Area $= \pi r_i^2$			A_f	Fin Surface Area $= L \times W$
	A_e	Evapor. Surface Area $= 2\pi r_o l_e$					A_c	Condenser Radiative Area $= 2 r_o l_c$

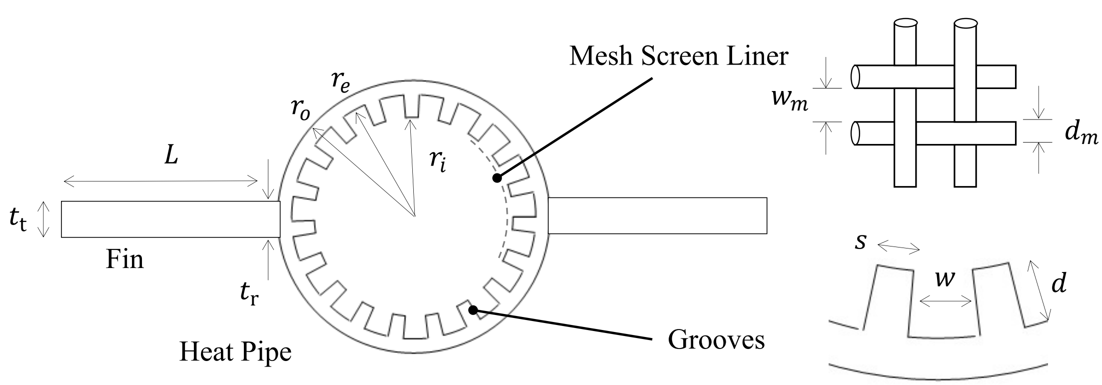

Fig. 4 Geometry of heat pipe, radiator fin and mesh screen liner.

The implicit variables shown in Table 3 include cross-sectional areas and surface areas useful for understanding the formulas below, but don't include other variables such as volumes and mass fractions that are also evaluated at each design iteration. These variables are taken as elementary in calculation. However, there are a number of calculated parameters related to wicks that require specific consideration.

C. Wick Calculated Parameters

Different wick designs can be compared using a normalized set of performance parameters; $\psi, D_h, r_{\text{eff}}, K$ and k_{eff}, but each wick evaluates these parameters differently depending on the geometry inputs. Table 4 shows the relevant equations for finding these parameters across four different wick types. Porosity is also known as the *liquid void fraction* and is the relative fraction of the wick's wetted area that is filled with fluid under regular operating conditions. It is used in conjunction with density and volume to calculate the mass fraction of each component within the wick. With porosity and hydraulic diameter we can define the most important properties for assessing heat pipes, and for which we need to perform trade studies;

- Effective Pore Radius r_{eff} - a measure of the surface area delineating the fluid and vapor regimes at the evaporator, which sets the available pressure head due to the surface tension.
- Permeability K - the inverse of resistance when considering the ability of the fluid to transverse from the condenser to the evaporator.
- Effective Thermal Conductivity k_{eff} - which is found combining the thermal conductivities of the solid, fluid, and the wick geometry. *It is not the same* as the conductance implied by the evaporative performance of the heat pipe as a whole.

Typically, the pore radius and permeability are at odds, as the more open (i.e. permeable) a wick design, the greater the surface area at the fluid-vapor interface and thus a lower available pressure [2]. This effect is overcome if the wick is anisotropc along the radial and axial dimensions, and can be achieved through the use of a mesh screen layered on top of the grooves. In this case, r_{eff}, K and k_{eff} are defined by the closest approximation of either the groove or mesh screen design (see Groove-mesh hybrid in Table 4). Such a construction has been used in traditional manufacturing [21, 22], and additive manufacturing will make even more complex topologies available [23] though we are using this model to represent an ideal case in the first instance.

Table 4 Calculated parameters for heat pipe performance [2].

Wick Style	ψ (-)	D_h (m)	r_{eff} (m)	K (m^2)	k_{eff} (W/m·K)
Grooved	$\dfrac{w}{(t+w)}$	$\dfrac{dw}{2(d+w)}$	w	$\dfrac{D_h^2\psi}{2(f\,\text{Re}_{l,h})}$	$k_s(1-\psi(1-\dfrac{k_f}{k_s}))$
Sintered*	ψ	$\dfrac{D\psi}{1-\psi}$	$0.21D$	$\dfrac{D^2\psi^3}{150(1-\psi^2)}$	$k_s\dfrac{2+k_f/k_s-2\psi(1-k_f/k_s)}{2+k_f/k_s-\psi(1-k_f/k_s)}$
Mesh Screen†	$1-\dfrac{1.05\pi N d_m}{4}$	$\dfrac{d_m\psi}{1-\psi}$	$\dfrac{w_m+d_m}{2}$	$\dfrac{D^2\psi^3}{122(1-\psi^2)}$	$k_f\dfrac{k_f+k_s-(1-\psi)(k_f-k_s)}{k_f+k_s+(1-\psi)(k_f-k_s)}$
Groove Mesh Hybrid†	$\dfrac{w}{(t+w)}$	$\dfrac{dw}{2(d+w)}$	$\dfrac{w_m+d_m}{2}$	$\dfrac{D_h^2\psi}{2(f\,\text{Re}_{l,h})}$	$k_s(1-\psi(1-\dfrac{k_f}{k_s}))$

*D-Powder Sphere Diameter   † N-Mesh Number

D. Heat Pipe Performance Limits

This section describes the five heat pipe performance limits evaluated in the model. For a deeper exploration see Faghri [2]. In the present study, as in many heat pipes, performance is dominated by the *capillary limit*. For a given temperature, a wick can transport a maximum mass flow based on its permeability and the driving pressure. Taking the product of this mass flow and the enthalpy of vaporization gives the capillary heat load limit;

$$Q_c = \frac{\rho_l \sigma h_{\text{fg}}}{\mu_l}\frac{K A_w}{l_{\text{eff}}}\left(\frac{2}{r_{\text{eff}}} - \frac{\rho_l g l_t}{\sigma}\cos(\theta)\right) \tag{2}$$

where the last term represents the gravitational pressure working against a heat pipe inclined at an angle θ. This term is not significant in horizontal heat pipes nor in space applications. Note that the fluid merit number M is embedded at the start of this equation, and so demonstrates why M is used to compare potential working fluids. Other limits considered in this work are the;

$$\text{Boiling limit} \quad Q_b = \frac{4\pi(l_e)k_{\text{eff}}\sigma T_v}{h_{\text{fg}}\rho_l \ln(r_s/r_i)}\left(\frac{1}{r_n} - \frac{1}{r_{\text{eff}}}\right) \tag{3}$$

$$\text{Entrainment limit} \quad Q_e = A_v h_{\text{fg}}\left(\frac{\rho_v \sigma}{2r_{\text{cav}}}\right)^{0.5} \tag{4}$$

$$\text{Viscous limit} \quad Q_v = \frac{\pi r_i^4 h_{\text{fg}}\rho_v P_v}{12\mu_l l_{\text{eff}}} \tag{5}$$

$$\text{Sonic limit} \quad Q_s = 0.474 A_v h_{\text{fg}}\left(\rho_v P_v\right)^{0.5} \tag{6}$$

For instance, the *boiling limit* occurs when high heat flux at the evaporator leads to bubble nucleation within the wick structure (rather than at the vapor core boundary) which inhibits the full flow and wetting of the evaporator end. This often occurs when operating near the fluid's critical temperature but is also dependent on the envelope properties. The *entrainment limit* is an example of a limit that can impede HP efficacy, without necessarily halting the process entirely. This occurs when the speed of the vapor flow creates significant shear stress at at vapor-fluid boundary along the length of the HP. The *viscous limit* reflects the restriction caused by a fluid's increased viscosity at low temperatures. Finally, at similarly low temperatures, the *sonic limit* represents the restriction caused by a limited vapor fraction reaching sonic velocities when traversing the axial length of the vapor core.

The performance envelope $Q_{\text{env}}(T)$ is evaluated as the minimum value of the above for the temperature range under consideration as seen in Fig. 5.

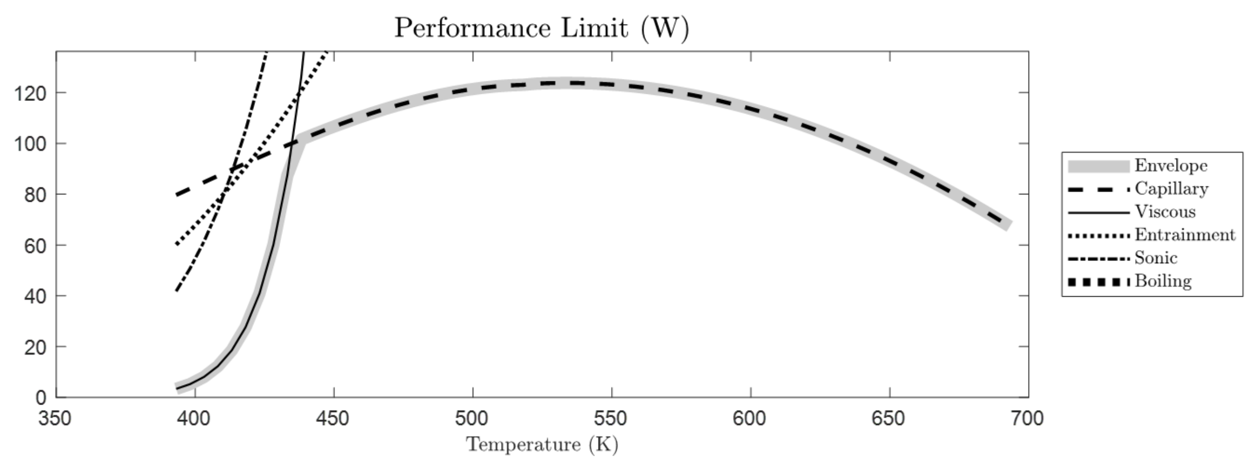

Fig. 5 Example of heat pipe performance envelope as minimum of other performance limits.

E. Radiative Heat Transfer

The radiative areas are comprised of the two fins and the exposed length of the heat pipe's condenser section. The condenser section is modeled as if it were a flat plate with one-sided area A_c. This conservative approximation of the area allows us to neglect any possible view factor between the condenser and the fins. The condenser is also treated as isothermal. The total heat radiated (from both sides) is then given;

$$Q_{\text{hp,rad}} = 2 \times A_c \sigma_{\text{SB}} \epsilon (T_{\text{hp}}^4 - T_\infty^4) \tag{7}$$

The temperature profile along the length of the radiator fin is modeled using a one-dimensional finite-difference method, with elements of length Δx, thickness t and width W (see Fig. 6). In this analysis, the temperature is assumed constant along the fin's width*. The heat equation for this profile is;

$$\frac{dT}{dt} = \alpha \frac{d^2T}{dx^2} + \frac{Q_{\text{rad}}(x,t)}{dm} \tag{8}$$

Thus, in the finite-difference method, the temperature of element i at the timestep j can be solved via;

$$T_i^{j+1} = T_i^j + \frac{\Delta t}{c_p \rho W t} \left(\frac{kA_x}{\Delta x^2} (T_{i-1}^j - 2T_i^j + T_{i+1}^j) + 2\sigma_{\text{SB}} \epsilon W ((T_i^j)^4 - T_\infty^4) \right) \tag{9}$$

The boundary conditions at steady state are that the root temperature ($x = 0$) is equal to heat pipe operating condition, and that the heat conducted into the tip ($x = L$) must all be radiated out. at the root and tip given by, respectively;

$$T_0 = T_{\text{hp}} \tag{10}$$

$$-kt_t \frac{dT}{dx}|_L = 2\sigma_{\text{SB}} \epsilon (T_L^4 - T_\infty^4) \tag{11}$$

The time step Δt is evaluated based on the Mesh Fourier number;

$$\text{Fo}_M = \frac{\alpha \Delta t}{\Delta x^2} \leq \frac{1}{2} \tag{12}$$

By keeping this inequality satisfied, we can maintain stability in the solution. Though this algorithm is inherently transient, we are only interested in the steady-state solution, but it is numerically advantageous to use this approach. Finally, we evaluate the heat radiated from the fin by summing over the elements;

$$Q_{\text{fin,rad}} = \sum 2\sigma_{\text{SB}} \epsilon W \Delta x \left(T_i^4 - T_\infty^4 \right) \tag{13}$$

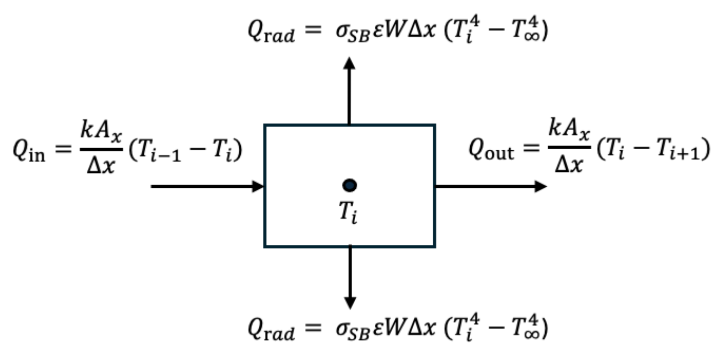

Fig. 6 Heat flow into a finite element control volume that spans the fin width.

F. Radiator Performance Metrics

The parameters in Table 5 are useful to compare overall radiator performance across designs, and are vital to the optimization strategy detailed in the next section. The absolute parameters are the total mass, total radiating area, and total radiating power of the combined system. Together, they provide scalable parameters for comparison design comparison and full-scale evaluation. The *areal density* is a simple measure of the mass per unit radiating area (kg/m^2) which is typically minimized where possible. According to the NASA Civil Shortfalls documentation, an optimistic target is <3 kg/m^2. The *power density* (or heat flux) is used to evaluate the thermal power delivered per unit area. Combining these gives the *heat rejection specific mass*, with a target of <1 kg/kW for NEP systems.

*Note that the "length" of the fin is measured from the root, hence it is perpendicular to the orientation of the heat pipe "length"

Table 5   **Heat pipe radiator performance metrics.**

Absolute			Scaled		
Total Mass	m_{tot}	$= m_{\text{hp}} + m_{\text{fluid}} + 2m_{\text{fin}}$	Areal Density	ρ_A	$= \frac{m_{\text{tot}}}{A_{\text{tot}}}$
Total Radiating Area	A_{tot}	$= A_c + 2A_f$	Power Density	ϕ	$= \frac{Q_{\text{tot}}}{A_{\text{tot}}}$
Total Radiating Power	Q_{tot}	$= Q_{\text{hp,rad}} + 2Q_{\text{fin,rad}}$	Heat Rejection Specific Mass	β	$= \frac{m_{\text{tot}}}{Q_{\text{tot}}}$
			Radiator Efficiency	η	$= \frac{Q_{\text{tot}}}{Q_{\text{ideal}}}$

The *radiator efficiency* is defined by the power rejection from the radiator divided by the power rejection of an ideal radiator operating at a constant maximum temperature (e.g. T_{hp}). A final metric is the *evaporator flux* (Q_{tot}/A_e) that represents the convective heat transfer at the evaporator end. It is outside the scope of this effort, though it is monitored as typically <20 W/cm^2, and is representative of the boiling limit in effect.

V. Optimization

A. Objective Function

The objective function of the optimization algorithm is to minimize the areal density of the heat pipe radiator. The algorithm uses Matlab's Sequential Quadratic Programming method to identify local minima, but can get stuck in local minima due to the non-linear constraints. To overcome this, it employs a basin-hopping approach using Matlab's global search function to escape the local minima and locate the global minimum. A description is given by Schittkowski [24] and a full review of optimization algorithms for heat pipes is given by Tian [13].

B. Parameters and Constraints

The optimization parameters are the independent geometric variables of the radiator and heat pipe. In total, there are 13 optimization parameters which are listed in Table 3. The constraints for the optimization include both performance and geometric constraints. Some of the important constraints are shown in Table 6. Performance constraints were initially derived from the NASA Civil Shortfalls documentation and rule-of-thumb practicality (in the case of η). The geometric constraints ensure that the solution is valid topologically. The added 0.5 mm difference between the radii is to ensure some minimal thickness concordant with the present state of the additive manufacturing research. In future work, this constraint will be modeled on the structural integrity of the AlN envelope properties and the expected pressure vessel stress.

Table 6   **Selection of performance and geometric constraints for optimization.**

Performance Constraints		Geometry Constraints	
ρ_A	< 3 kg/m^2	$r_e + 0.5$mm	$< r_o$
β	< 1 kg/kW	$r_i + 0.5$mm	$< r_e$
η	$> 70\%$	t_t	$< t_r$

VI. Results

A. Initial Optimization from Baseline

The global optimization algorithm defined in this work achieved significant improvements in the radiator design compared to previous simulations. As a baseline, the final design described by Van Paridon et al. [19] is considered. This baseline model utilized AlN as both the heat pipe envelope and radiator material, with $AlBr_3$ as the working fluid. The results of this baseline design are presented in Fig. 7.

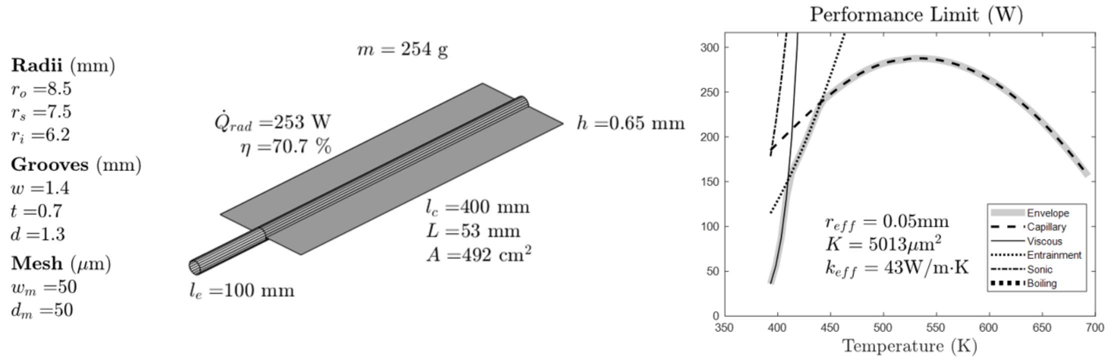

Fig. 7 Baseline design of AlN radiator *left* and HP performance envelope *right*. This design has ρ_A = 5.2 kg/m^2, ϕ = 7.4 kW/m^2, and β = 0.71 kg/kW.

By utilizing the same material and working fluid while allowing the optimization algorithm to determine the global minimum of areal density, the performance of the heat pipe and radiator system is significantly improved, as shown in Fig. 8.

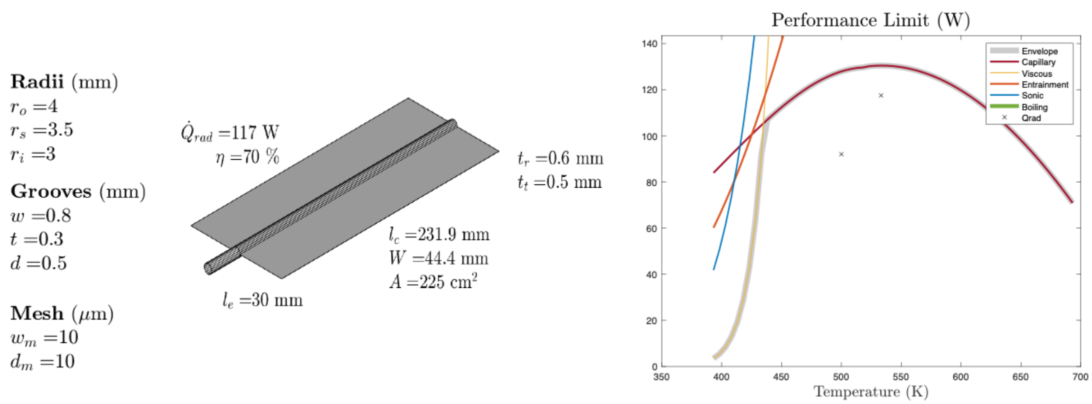

Fig. 8 Optimized Design of AlN HP Radiator *left* and Performance Envelope *right*. This design has ρ_A = 2.4 kg/m^2, ϕ = 5.23 kW/m^2, and β = 0.46 kg/kW.

The optimized geometry demonstrates a significant improvement over the baseline design, with the areal density decreasing from 5.2 kg/m^2 to 2.4 kg/m^2 (-53.8%). This first finding is that, using geometric optimization, designs achieving an areal density below 3 kg/m^2 are feasible. Further enhancements in material selection and working fluid optimization could potentially lower this value even more.

Scrutiny of the results reveals that several parameters tend toward the lower bound set for the optimization scope. These include the thickness of heat pipe and radiator features, and the evaporator length. This is expected, as the required wall thickness is largely determined by the structural integrity achievable within the material, while the evaporator length depends on the convective heat transfer from the pumped fluid loop.

B. Sensitivity to Effective Pore Radius

Screen mesh thicknesses (w_m, d_m) also tend toward their minimum bounds, significantly influencing the effective pore radius (r_{eff}), which in turn impacts the capillary limit of the heat pipe. These mesh features act as a proxy for the r_{eff} achievable through additive manufacturing. To investigate further, the lower bound of r_{eff} was varied, with all other parameters optimized globally. Results, presented in Table 7, show strong correlation with heat pipe length, but minimal impact on other key performance parameters, including overall width. From a practical standpoint, larger radiator sections simplify installation by reducing the number of components needed to achieve the required radiative area.

Overall, these results suggest that thinner and finer radiator designs are preferable, with the effective pore radius (r_{eff}) serving as the primary determinant of optimal heat pipe length. However, it should be noted that the current model does not incorporate penalties for installation, which would typically scale inversely with radiator size.

Table 7 Sensitivity of AlN-AlBr$_3$ heat pipe performance to r_{eff} .

r_{eff}	(μm)	10	20	30	40	50	60
L_{rad}	(mm)	227	154	122	103	90.6	76.3
W_{rad}	(mm)	96.5	96.8	96.7	96.1	96.0	97.0
Q_{rad}	(W)	112	76	60	51	45	38
$Q_{\text{hp,limit}}$	(W)	133	90	71	60	53	45
m_{tot}	(g)	53	37	30	26	23	20
ρ_A	(kg/m^2)	2.4	2.5	2.5	2.6	2.6	2.7
ϕ	(kW/m^2)	5.1	5.1	5.1	5.1	5.1	5.1
β	(kg/kW)	0.47	0.49	0.5	0.51	0.52	0.53
η	(%)	72.3	72.3	72.3	72.3	72.3	72.4

C. Radiator Material Trade Study

A trade study on the radiator material was performed by running the optimization algorithm for four different materials and their properties. The four materials we evaluated were AlN, K1100 (a carbon fiber composite), graphite, and graphene, with properties shown in Table 8.

Table 8 Relevant thermal properties of radiator materials

Properties	AlN	K1100	Graphite Sheet	Graphene Sheet
Density (kg/m^3)	3255	1812	1500	2267
Thermal Conductivity (W/m/K)	130	600	400	2000
Specific Heat (J/kg/K)	740	2000	780	1250
Thermal Diffusivity (10^{-5} m^2/s)	5.40	16.56	34.19	70.58

The results of the material trade study shown in Table 9 and are illustrated in Fig. 9. The first four columns show the results for the different materials. In each case, the heat pipe has the same geometric constraints, and all designs tend towards the minimum thickness allowed. This leads to the unexpected result that graphite appears to outperform graphene, whereas this would likely not be true if appropriate structural limits on thickness were employed. These results show that the material choice will impact the overall ratio and dimensions of the radiator, but not greatly impact the power density.

Table 9 Sensitivity of AlN-AlBr$_3$ heat pipe performance to radiator material.

Material		AlN	K1100	Graphite	Graphene	
						(t_r/2)
L_{rad}	mm	227	213	171	110	121
W_{rad}	mm	96	97	163	355	299
Q_{rad}	W	112	105	140	194	181
$Q_{\text{hp,limit}}$	W	133	139	166	230	215
m_{tot}	g	53	44	36	56	38
ρ_A	kg/m2	2.4	2.2	1.3	1.4	1.0
ϕ	kW/m2	5.11	5.11	5.03	4.98	4.98
β	kg/kW	0.47	0.42	0.25	0.29	0.21
η	%	72.3	72.3	71.3	70.5	70.6

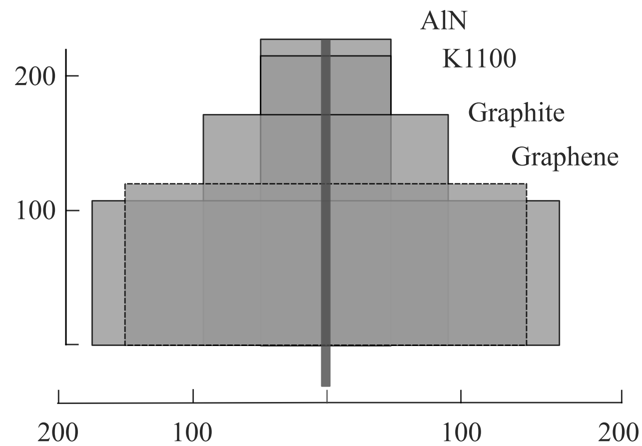

Fig. 9 Overlay of optimized radiator fins for different materials using the same input parameter bounds.

Furthermore, since all materials evaluated meet the desired performance for areal density, the added complexity of using alternative materials may not be justified. A key consideration in implementing these materials is the mismatch in the coefficient of thermal expansion between the radiator and AlN. Addressing this mismatch would require novel manufacturing and binding techniques to fully realize the performance benefits, and the additional assembly processes could potentially offset the gains achieved by using these materials.

VII. Conclusions

A comprehensive model of a heat pipe and radiator assembly is presented, enabling the prediction and optimization of system performance for various working fluids and envelope materials. Through this model, we demonstrated the feasibility and potential performance of an AlN-$AlBr_3$ radiator as a key component in future nuclear propulsion systems. The findings suggest that the additive manufacturing process used to create the heat pipe envelope is a critical factor in determining system performance. In particular, the achievable pore radius strongly influences the optimal heat pipe length while having minimal impact on overall performance. Similarly, the thermal diffusivity of the fin material dictates the ratio of length to width. While materials with a thermal expansion coefficient mismatch with AlN pose potential challenges in construction, these challenges could be mitigated by additive manufacturing the entire structure as a single monolithic piece. This approach simplifies assembly and ensures that performance remains superior to required levels. The key design principle identified is to thin down ceramic components wherever feasible to reduce mass and enhance performance.

Future work will integrate experimental efforts to refine structural parameters and gather validation data, driving iterative design improvements. To date, rate-of-rise testing has been conducted to determine the permeability of AlN heat pipes using ethanol and Dowtherm A, as detailed in [20]. The observed permeability values, ranging from 800-1500μm^2, closely align with the modeling predictions, reinforcing confidence in the model's accuracy. Continued model development and experimental validation will further advance the feasibility of employing additive manufacturing techniques to develop cutting-edge heat pipe and radiator systems, which are essential for next-generation space missions.

Acknowledgments

This work was supported by the NASA Early Stage Innovations grant (grant number 80NSSC23K0236). The authors also acknowledge the use of facilities and instrumentation funded by the National Science Foundation through the Cornell University Materials Research Science and Engineering Center (DMR-1719875). Special thanks are extended to William Sixel for their insightful discussions.

References

[1] Mason, L. S., Oleson, S. R., Jacobson, D. T., Schmitz, P. C., Qualls, L., Smith, M., Ade, B., and Navarro, J., "Nuclear Power Concepts and Development Strategies for High-Power Electric Propulsion Missions to Mars," *NASA Office of Strategic Engagement and Assessments*, 2022. URL `https://ntrs.nasa.gov/citations/20210016968`.

[2] Faghri, A., "Heat Pipes and Thermosyphons," *Handbook of Thermal Science and Engineering*, 2018, pp. 2163–2211.

[3] Werner, T. C., Yan, Y., Karayiannis, T., Pickert, V., Wrobel, R., and Law, R., "Medium temperature heat pipes – Applications, challenges and future direction," , 1 2024. https://doi.org/10.1016/j.applthermaleng.2023.121371.

[4] Anderson, W. G., Tarau, C., and Ellis, D. L., "Intermediate Temperature Heat Pipe Working Fluids," *Heat Pipes: Design Applications and Technology*, 2018, pp. 395–423.

[5] Anderson, W. G., Bonner, R. W., Dussinger, P. M., Hartenstine, J. R., Sarraf, D. B., and Locci, I. E., "Intermediate Temperature Fluids Life Tests-Experiments," *5th International Energy Conversion Engineering Conference and Exhibit (IECEC)*, 2007.

[6] Sommers, A., Wang, Q., Han, X., T'Joen, C., Park, Y., and Jacobi, A., "Ceramics and ceramic matrix composites for heat exchangers in advanced thermal systems—A review," *Applied Thermal Engineering*, Vol. 30, No. 11, 2010, pp. 1277–1291. https://doi.org/10.1016/j.applthermaleng.2010.02.018, URL https://www.sciencedirect.com/science/article/pii/S1359431110000773.

[7] Cramer, C. L., Lara-Curzio, E., Elliott, A. M., Aguirre, T. G., Yoon, B., Fricke, B. A., Rao, V., Jain, P., and Nawaz, K., "Material selection and manufacturing for high-temperature heat exchangers: Review of state-of-the-art development, opportunities, and challenges," *International Journal of Ceramic Engineering & Science*, Vol. 6, No. 5, 2024, p. e10230. https://doi.org/10.1002/ces2.10230, URL https://onlinelibrary.wiley.com/doi/abs/10.1002/ces2.10230, _eprint: https://ceramics.onlinelibrary.wiley.com/doi/pdf/10.1002/ces2.10230.

[8] Ababneh, M. T., Tarau, C., Andersont, W. G., Farmer, J. T., Alvarez-Henandez, A. R., and Ortega, S., "Advanced passive thermal experiment for hybrid variable conductance heat pipes and high conductivity plates on the international space station," *47th International Conference on Environmental Systems*, 2017. URL http://hdl.handle.net/2346/73058.

[9] Hack, N., Unz, S., and Beckmann, M., "Ceramic Heat Pipes for High Temperature Application," *Energy Procedia*, Vol. 120, 2017, pp. 140–148. https://doi.org/10.1016/j.egypro.2017.07.147, URL https://www.sciencedirect.com/science/article/pii/S1876610217327133.

[10] Sixel, W., Kaviany, M., and Leary, A., "Ceramic Heat Pipe for Thermal Management of a High-Frequency Inductor," *AIAA Propulsion and Energy 2021 Forum*, AIAA Propulsion and Energy Forum, American Institute of Aeronautics and Astronautics, 2021. https://doi.org/10.2514/6.2021-3335, URL https://arc.aiaa.org/doi/10.2514/6.2021-3335.

[11] Sixel, W., Kaviany, M., Hwang, G., and Egbo, M. K., "Experimental Demonstration and Characterization of a Ceramic Sintered Wick Heat Pipe Evaporator," *AIAA AVIATION 2023 Forum*, AIAA AVIATION Forum, American Institute of Aeronautics and Astronautics, 2023. https://doi.org/10.2514/6.2023-3878, URL https://arc.aiaa.org/doi/10.2514/6.2023-3878.

[12] Agrawal, P., Ahmadi, B., Cesarano, J., and Bigham, S., "3D-printed Ceramic Oscillating Heat Pipes for Improved Electronic Thermal Management," *2024 23rd IEEE Intersociety Conference on Thermal and Thermomechanical Phenomena in Electronic Systems (ITherm)*, 2024, pp. 1–5. https://doi.org/10.1109/ITherm55375.2024.10709538, URL https://ieeexplore.ieee.org/abstract/document/10709538?casa_token=6n_tT9m7vN0AAAAA:e3NkfH7t7hQiWj0Hth9f5lGKm76VxghH9Z8ORfydCmErb_8HO6lVbTJ8YtS6VnKfMK5swUx1nw, iSSN: 2694-2135.

[13] Tian, Z., Wang, C., Guo, K., Zhang, D., Su, G., Tian, W., and Qiu, S., "A review of liquid metal high temperature heat pipes: Theoretical model, design, and application," *International Journal of Heat and Mass Transfer*, Vol. 214, 2023, p. 124434. https://doi.org/https://doi.org/10.1016/j.ijheatmasstransfer.2023.124434, URL https://www.sciencedirect.com/science/article/pii/S0017931023005793.

[14] Nemec, P., Čaja, A., and Malcho, M., "Mathematical model for heat transfer limitations of heat pipe," *Mathematical and Computer Modelling*, Vol. 57, No. 1, 2013, pp. 126–136. https://doi.org/10.1016/j.mcm.2011.06.047, URL www.sciencedirect.com/science/article/pii/S0895717711003888.

[15] Furukawa, M., "Design and off-design performance calculations of space radiators," *Journal of Spacecraft and Rockets*, Vol. 18, No. 6, 1981, pp. 515–526. https://doi.org/10.2514/3.28067, URL https://doi.org/10.2514/3.28067.

[16] Hull, P. V., Kittredge, K., Tinker, M. L., and SanSoucie, M. P., "In-Space Radiator Shape Optimization using Genetic Algorithms," 2006. URL https://api.semanticscholar.org/CorpusID:106589226.

[17] Juhasz, A. J., "Design Considerations for Lightweight Space Radiators Bases on Fabication and Test Experience With a Carbon-Carbon Composite Prototype Heat Pipe," 1998. URL https://ntrs.nasa.gov/api/citations/19980236936/downloads/19980236936.pdf.

[18] D’Orazio, G., Sixel, W. R., and Sobhani, S., “Additive Manufacturing and Working Fluid Characterization of Ceramic Heat Pipes,” *AIAA SCITECH 2024 Forum*, 2024. https://doi.org/10.2514/6.2024-1792, URL https://arc.aiaa.org/doi/abs/10.2514/6.2024-1792.

[19] van Paridon, A., D’Orazio, G., Sixel, W. R., and Sobhani, S., “Intermediate Temperature Ceramic Heat Pipe Modeling and Optimization,” *Thermal and Fluids Analysis Workshop (TFAWS)*, 2024.

[20] D’Orazio, G., van Paridon, A., Petro, E., and Sobhani, S., “Development and Testing of Grooved Aluminum Nitride Heat Pipes for Intermediate Temperature Systems,” *AIAA SCITECH 2025 Forum*, 2025.

[21] Wong, S.-C., Deng, M.-S., and Liu, M.-C., “Characterization of composite mesh-groove wick and its performance in a visualizable flat-plate heat pipe,” *International Journal of Heat and Mass Transfer*, Vol. 184, 2022, p. 122259. https://doi.org/https://doi.org/10.1016/j.ijheatmasstransfer.2021.122259, URL https://www.sciencedirect.com/science/article/pii/S0017931021013582.

[22] Krambeck, L., Bartmeyer, G., Santos, P., and Antonini Alves, T., “Experimental Analysis of a Screen-Covered Groove Heat Pipe,” *Revista de Engenharia Térmica*, Vol. 17, 2018, p. 58. https://doi.org/10.5380/reterm.v17i1.62259.

[23] Hasan, M., Elkholy, A., Narvan, M., Durfee, J., and Kempers, R., “Capillary performance of strut-based lattice wicks fabricated using laser powder bed fusion,” *International Communications in Heat and Mass Transfer*, Vol. 159, 2024, p. 108227. https://doi.org/https://doi.org/10.1016/j.icheatmasstransfer.2024.108227, URL https://www.sciencedirect.com/science/article/pii/S0735193324009898.

[24] Schittkowski, K., “Nonlinear Programming: Algorithms, Software, and Applications,” 1985. https://doi.org/10.1007/0-387-23467-5_5, URL https://www.researchgate.net/publication/227324400_Nonlinear_Programming_Algorithms_Software_and_Applications.